

See discussions, stats, and author profiles for this publication at: <https://www.researchgate.net/publication/274084485>

Crashworthiness design for functionally graded foam-filled bumper beam

Article in *Advances in Engineering Software* · July 2015

DOI: 10.1016/j.advengsoft.2015.03.005

CITATIONS

121

READS

2,268

4 authors:



Zhi Xiao

Hunan University

34 PUBLICATIONS 749 CITATIONS

SEE PROFILE



Jianguang Fang

University of Technology Sydney

127 PUBLICATIONS 6,115 CITATIONS

SEE PROFILE



Guangyong Sun

Hunan University

257 PUBLICATIONS 16,517 CITATIONS

SEE PROFILE

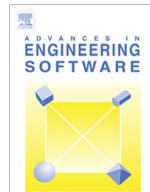


Qing Li

The University of Sydney

528 PUBLICATIONS 24,787 CITATIONS

SEE PROFILE



Crashworthiness design for functionally graded foam-filled bumper beam



Zhi Xiao^a, Jianguang Fang^{b,c}, Guangyong Sun^{a,c,*}, Qing Li^c

^a State Key Laboratory of Advanced Design and Manufacture for Vehicle Body, Hunan University, Changsha 410082, China

^b School of Automotive Studies, Tongji University, Shanghai 201804, China

^c School of Aerospace, Mechanical and Mechatronic Engineering, The University of Sydney, Sydney, NSW 2006, Australia

ARTICLE INFO

Article history:

Received 17 November 2014

Received in revised form 5 February 2015

Accepted 1 March 2015

Available online 27 March 2015

Keywords:

Bumper beam

Functionally graded foam (FGF)

Crashworthiness

Energy absorption

Multiobjective optimization

Kriging model

ABSTRACT

Automotive bumper beam is an important component to protect passenger and vehicle from injury and damage induced by severe collapse. Recent studies showed that foam-filled structures have significant advantages in light weight and high energy absorption. In this paper, a novel bumper beam filled with functionally graded foam (FGF) is considered here to explore its crashworthiness. To validate the FGF bumper beam model, the experiments at both component and full vehicle levels are conducted. Parametric study shows that gradient exponential parameter m that controls the variation of foam density has significant effect on bumper beam's crashworthiness; and the crashworthiness of FGF-filled bumper beam is found much better than that of uniform foam (UF) filled and hollow bumper beam. The multiobjective optimization of FGF-filled bumper beam is also performed by considering specific energy absorption (SEA) and peak impact force as the design objectives, and the wall thickness t , foam densities ρ_1 and ρ_2 (foam densities at the end and at mid cross section, respectively) and gradient exponential parameter m as design variables. The Kriging surrogate modeling technique and multiobjective particle swarm optimization (MOPSO) algorithm were implemented to optimize the FGF-filled bumper beam. The optimized FGF-filled bumper beam is of great advantages and it can avoid the harmful local bending behavior and absorb more energy than UF filled and hollow bumper beam. Finally, the optimized FGF-filled bumper beam is installed to a passenger car model, and the results demonstrate that the FGF-filled bumper beam ensures the crashworthiness performance of the passenger car while reduces weight about 14.4% compared with baseline bumper beam.

© 2015 Elsevier Ltd. All rights reserved.

1. Introduction

Vehicle crashworthiness and lightweight design have attracted more and more attention by automobile manufactures and researchers [1,2]. Automotive bumper beam is the first component to undergo crashing deformation and a key part to ensure the crashworthiness performance of passenger cars. One of the main functions of the bumper beam is to transfer the impact load and energy to left and right side crash boxes and longitudinal rails as uniformly as possible, thereby decreasing the deformation on side during vehicle frontal impact especially frontal offset impact. Therefore, its design signifies a critical issue for entire vehicle.

Traditionally, bumper beam is a hollow thin-wall structure made of steel sheet or aluminum extrusion. During the impact,

the hollow bumper beam undergoes a bending collapse mode, which is typically localized in a small area and the other parts of the bumper beam experiences almost a rigid body rotation. In this regard, some studies on the bending behavior of thin walled beams were reported. A comprehensive investigation into the bending performance of square and rectangular prismatic beams was conducted by Kecman [3]. Wierzbicki et al. [4] derived the mathematical equations to predict the bending resistances of thin-walled box sectional beams. Liu and Day [5] also investigated the bending characteristics of thin-walled channel section beams.

Due to the localized bending deformation, the resistance force drops drastically after bending collapse and the energy absorbing ability is fairly low [6]. The presence of foam material in thin-walled structures seems to be a proper solution to enhance structural rigidity and reduce localized bending deformation for better energy absorption [7,8]. In this respect, ultra-light cellular metals such as aluminum foams have been considered an ideal filler material in the thin-walled structures on account of their low density,

* Corresponding author at: State Key Laboratory of Advanced Design and Manufacture for Vehicle Body, Hunan University, Changsha 410082, China. Tel.: +86 731 8881 1445; fax: +86 731 8882 2051.

E-mail address: sgy800@126.com (G. Sun).

high stiffness, good impact resistance, high energy absorption capacity, and easy to manufacture [9,10]. Wierzbicki and his coworkers [11,12] explored the effect of ultralight metal foam on the bending collapse behavior of thin-walled columns and drew a conclusion that filling aluminum honeycomb or foam core is preferable to enhance the energy-absorbing efficiency. Zarei and Kröger [13] performed bending crash tests and simulation for empty and foam-filled square beams, and they investigated the strengthening effect of foam and implemented the optimization technique to search for an optimum foam-filled beam. Guo and Yu [6] studied the dynamic bending responses of foam-filled bitubal structures experimentally and numerically and they found that foam-filled bitubal structure has a more stable load bearing capacity and much higher energy absorption efficiency in comparison with the traditional foam-filled single tube. Duarte et al. [14] studied dynamic and quasi-static 3-point bending responses of foam-filled tubal structures experimentally and concluded that foam filler changes the transverse crashing mode and allows generating a higher load carrying capacity and much higher energy absorption efficiency comparing with the empty counterpart. However, the practical application of foam-filler to bumper beam structure for a passenger car has not been reported yet in literature to date.

These abovementioned foam materials contain approximately uniform microscopic pores, namely uniform foam materials. Their overall characteristics are thus assumed to be isotropic and homogeneous. The shortcoming of uniform foam-filled structures is that the filled structures may not make the best use of the materials and cannot exert their maximum capacities for crashworthiness. It would be advantageous to explore functionally graded foam-filled bumper beam to maximize crashworthiness capacities and lightweight. Recently, Gupta and Ricci [15] and Gupta [16] fabricated functionally graded syntactic foam and showed experimentally that it could improve the energy absorption. Sun et al. [17] adopted single and multiobjective particle swarm optimization methods to seek optimal density gradient for functionally graded foam-filled thin-walled structures and the results indicate that the optimized functionally graded foam-filled thin-walled tube is superior to its uniform counterpart in overall crashworthiness. This study enabled us to believe that functionally graded foam (FGF) materials have significant potential to improve the crashworthiness. Attia et al. [18] investigated energy absorption characteristics of functionally graded foam-filled structures through both axial and lateral grading patterns and achieved an improvement of 12% in *SEA* over their uniform counterparts with the same mass. Yin et al. [19,20] investigated the energy absorption characteristics of functionally lateral graded foam (FLGF)-filled square and tapered tubes. The results show that FLGF-filled tubes can absorb more energy than uniform foam-filled tubes with the same weight in most of the considered cases.

However, the abovementioned FGF-filled structures are mainly used for axial loading conditions. For bumper beam, transverse bending is more common under frontal impact. It would be therefore interesting to explore the crashworthiness of FGF-filled bumper beam and their capabilities to improve crash safety performance. In this paper, a FGF-filled bumper beam of a passenger car was modeled and its crashworthiness characteristics were evaluated through both frontal impact against a rigid wall and offset impact against a deformable barrier. A layered FE model was developed to approximate the FGF filler in terms of a power law exponent m . The effects of foam density grading, foam density range and wall thickness on the crashworthiness are investigated. Then a multiobjective optimization is carried out to seek for a best possible design. It will show whether the bumper beam filled by the graded foam could provide a better crash performance than the uniform counterpart.

2. Finite element model and experimental validation

2.1. Crashworthiness criteria

2.1.1. Crashworthiness criteria for bumper beam

To evaluate the crashworthiness of bumper beam structure, such quantitative criteria as energy absorption (*EA*), specific energy absorption (*SEA*), peak crashing force (F_{max}) and crash force efficiency (*CFE*) are commonly used. The energy absorption can be formulated as:

$$EA(d) = \int_0^d F(x) dx \quad (1)$$

where d is the crash displacement and $F(x)$ is the impact force.

The specific energy absorbed *SEA* is defined as energy absorbed per unit mass of structure material and is a key criterion to evaluate energy absorption capabilities of different materials and structures [21].

$$SEA(d) = \frac{EA(d)}{mass} \quad (2)$$

The average force curve (F_{avg}) for a given deformation can be calculated as:

$$F_{avg}(d) = \frac{EA(d)}{d} \quad (3)$$

Another indicator in relation to energy absorption capacity is crash force efficiency (*CFE*), which can be defined as:

$$CFE = \frac{F_{avg}(d)}{F_{max}} \quad (4)$$

where F_{max} is the maximum impact force. *CFE* is an indicator to characterize the load consistency, a higher value of *CFE* indicates the better loading uniformity [22,23]. An ideal energy absorber thus has $CFE = 1.0$.

2.1.2. Crashworthiness criteria for passenger car

In order to evaluate the performance of FGF-filled bumper beam, a passenger car model was also utilized to investigate its influence on impact responses of the whole car. In this regard, standard crash tests and crashworthiness criteria will be used.

Offset deformable barrier (ODB) impact test at 64 km/h and rigid wall impact test at 50 km/h were considered to study the crashworthiness of passenger car. During the frontal impact, occupant responses are measured by such indices as *HIC* (head injury criteria), chest acceleration, chest deflection and femur loads [24,25]. These indices can be affected by the vehicle crash pulse, the extent of the intrusion into the occupant compartment, restraint system, vehicle interior configuration and stiffness [24]. In this study, crash pulse and intrusion into the occupant compartment were adopted to evaluate the crashworthiness of passenger car body [26].

In the frontal impact test, two triaxial accelerometers are mounted to the rocker panels at the base of the B-pillar for acceleration measurements. Generally speaking, higher car crash acceleration implies larger force exerted on occupants and results in higher injury risk of occupants [27]. For this reason, peak acceleration A_p is employed as one of the crashworthiness criteria of vehicle.

Besides the peak acceleration, acceleration pulse shape also has great influence on occupant injury outcomes. To evaluate the acceleration pulse shape, the pulse waveform efficiency (η) is defined as [24]:

$$\eta = \frac{v^2/2}{X \cdot A_p} \quad (5)$$

where v is the vehicle impact velocity, X is the dynamic crash length of vehicle. Ideally, the crash deceleration/acceleration versus time curve approaches a square pulse, and an optimal waveform has a pulse waveform efficiency (η) of 1.0.

The previous studies showed that high intrusion of occupant cabin will lead to greater occupant injury index [28]. Following instruction from EuroNCAP and C-NCAP, the displacements of A-pillar, steering column and pedals are employed to measure intrusion of the passenger car.

2.2. Finite element model and experimental validation

2.2.1. Geometrical configuration

In order to study the crashworthiness of FGF-filled bumper beam, a hollow steel bumper beam was used as the baseline model, whose geometrical configuration consists of curved bumper beam (1) and crash boxes (2) as shown in Fig. 1. The bumper beam includes an outer sheet (1a) of 1.2 mm thickness and an inner sheet (1b) of 1.0 mm thickness, and crash boxes are also composed of an outer sheet and an inner sheet with the same thickness of 1.6 mm. The bumper beam has an arc shape with a radius of 1490 mm and lateral length of 1155 mm, and the distance between inner sides of crash boxes is 924 mm as shown in Fig. 1.

2.2.2. Finite element model

The finite element analysis was conducted in explicit finite element code LS-DYNA. The thin-walled structures of bumper beam were modeled with the Belytschko–Tsay thin shell elements. The material of the bumper beam is steel B410LA with mechanical properties of density $\rho = 7.8 \times 10^3 \text{ kg/m}^3$, Young's modulus $E = 210 \text{ GPa}$, Poisson's ratio $\nu = 0.30$, initial yielding stress $\sigma_{y0} = 443 \text{ MPa}$. The material of crash boxes is steel B260LYD with initial yielding stress σ_{y0} of 344 MPa. The constitutive relation was based on an elastic–plastic material model with von Mises isotropic plasticity and plastic hardening. Strain rate effects were considered by defining stress–plastic strain curves of steel sheet under different strain rates which obtained by high speed dynamic stretch tests. Intermediate values were obtained by interpolation method. The stress–plastic strain curves of these two materials under different strain rates were obtained by high speed dynamic stretch tests, as shown in Figs. 2 and 3, respectively.

2.2.3. Experimental validation

The FE model of bumper beam was validated against the quasi static 3-point bending test. The PLS-L50B4 electrohydraulic servo system for component impact was used to load the bumper beam and crash boxes during the bending test. The crash box flanges were fixed on the operational platform, and the cylindrical

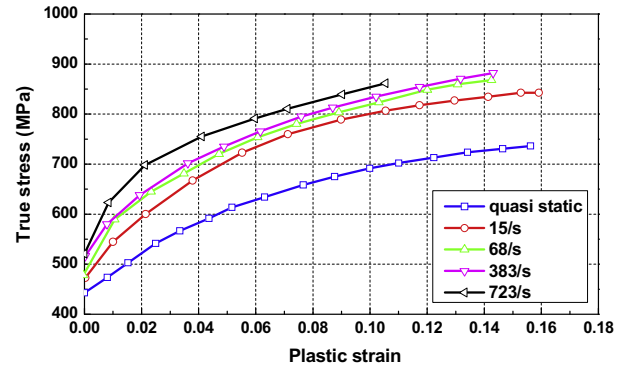


Fig. 2. True stress–plastic strain curves under different strain rates of B410LA.

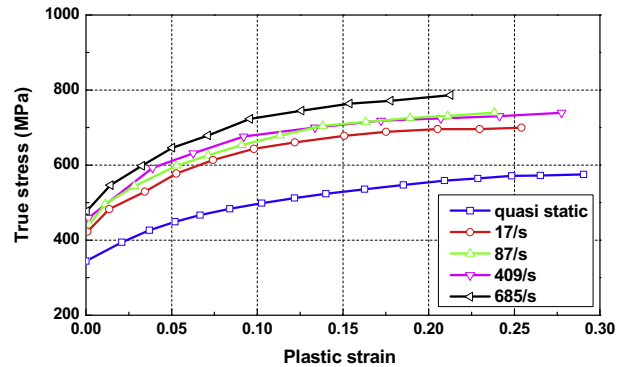


Fig. 3. True stress–plastic strain curves under different strain rates of B260LYD.

impactor with a radius of 152 mm was moved down until it contacted the middle part of the bumper beam, as shown in Fig. 4. The cylindrical impactor then moved down in a velocity of 0.001 m/s to press the bumper beam until the cylindrical impactor reached displacement of 100 mm.

According to the experimental test, the FE model of bumper beam was set up for a 3-point bending test in LS-DYNA code, as shown in Fig. 5. In order to reduce CPU time, the impactor velocity was set to 1 m/s in the FE model. In all the FE simulation cases of bumper beam, the impactor had the same displacement of 100 mm, and energy absorption was calculated while the impactor displacement reached 100 mm.

Fig. 6(a) displays the experimental results of bumper beam deformation and Fig. 6(b) shows the simulation results. The bumper beam undergoes in a localized bending deformation mode in

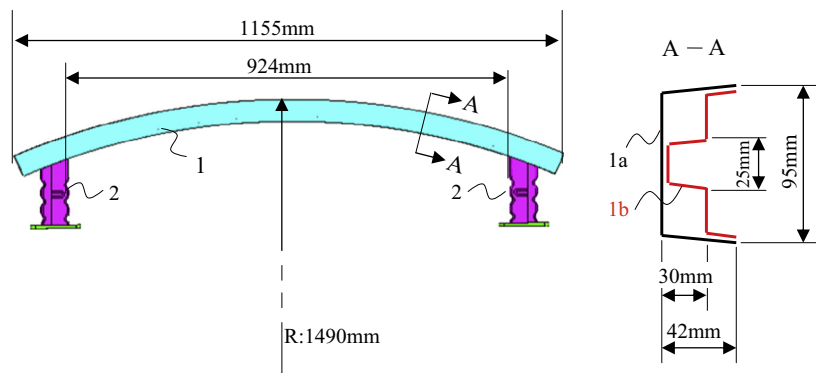


Fig. 1. Geometrical configuration of steel bumper beam.

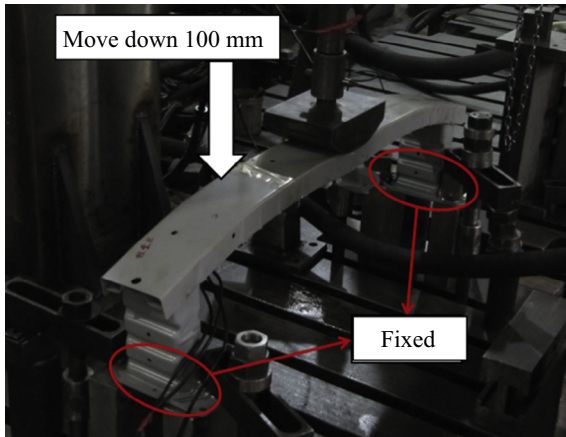


Fig. 4. Bending test of steel bumper beam.

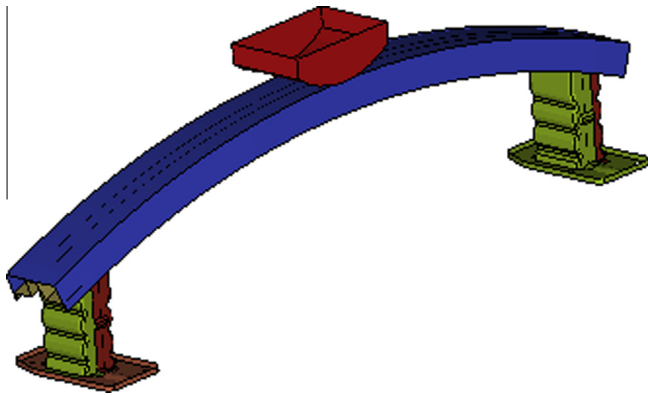


Fig. 5. Bending simulation of steel bumper beam.

both the experiment and simulation, and the deformation is concentrated in the mid section area where the impactor contacts. Note that the bending mode involves formation of local hinge, in which only small amount of material participates in deformation and energy absorption, thus it is a lower energy absorption mode.

Fig. 7 plots the relationship of impact force versus displacement of impact point at the bumper beam. The impact force increases

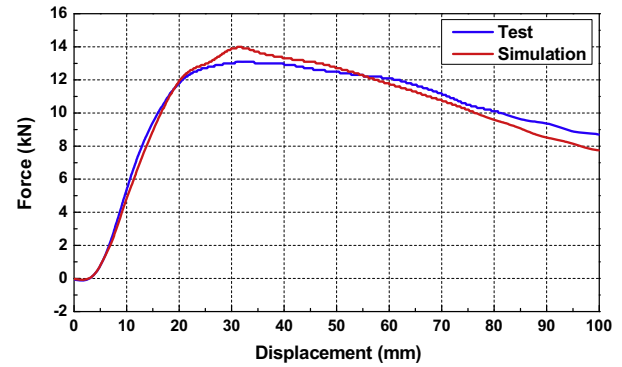


Fig. 7. Impact force versus displacement curve of hollow bumper beam.

gradually with the increase in the displacement before reaches a peak at $d = 30$ mm; then the impact force decreases when the displacement is greater than 30 mm due to local plastic deformation occurred. To reduce the localized bending mode, it would be beneficial to fill the bumper beam with foam materials, which will be discussed next section.

To study the performance of the foam-filled bumper beam in an entire car, a finite element model was also created, which has 1,087,070 elements and 1,056,355 nodes with a total mass of 1380 kg.

The test a frontal impact onto a rigid wall at 50 km/h and offset impact onto ODB (offset deformable barrier) at 64 km/h were conducted to validate the baseline model, which were implemented according to the C-NCAP and EuroNCAP protocols, respectively. Fig. 8 shows the car deformation of experiment and simulation during frontal rigid wall impact, where the deformation of FE model shows good agreement with that of experimental impact test. It is seen that in both the experiment and simulation the engine hood collapses in a similar bending mode, and passenger compartment maintains integrity because the doors, sill and A-pillar did not deform drastically. Fig. 9 plots the B-pillar acceleration history curves for the experiment and simulation under the frontal impact onto rigid wall. It can be seen that the acceleration pulse of FE model simulation is fairly consistent with that of rigid wall impact test.

Fig. 10 shows the deformations of test and simulation under the frontal offset impact, which shows a considerable agreement in the deformation modes. Fig. 11 plots the B-pillar acceleration history

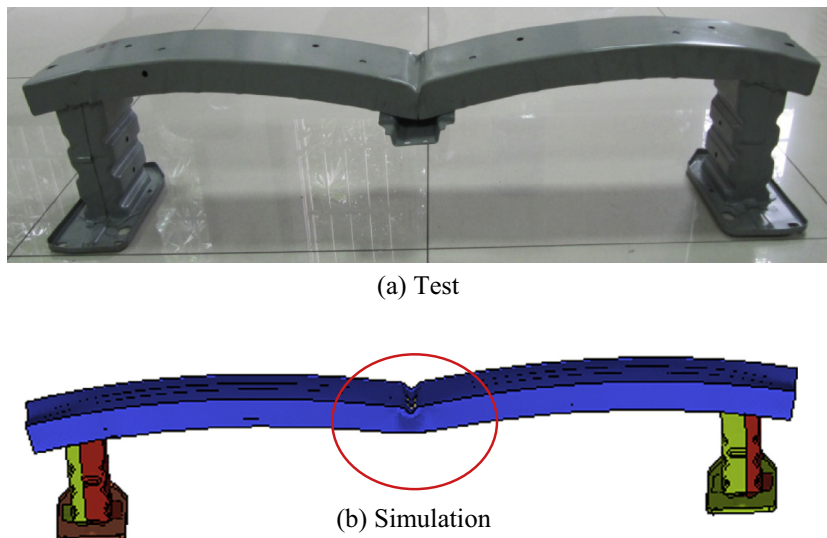


Fig. 6. Comparison of bumper beam deformation.

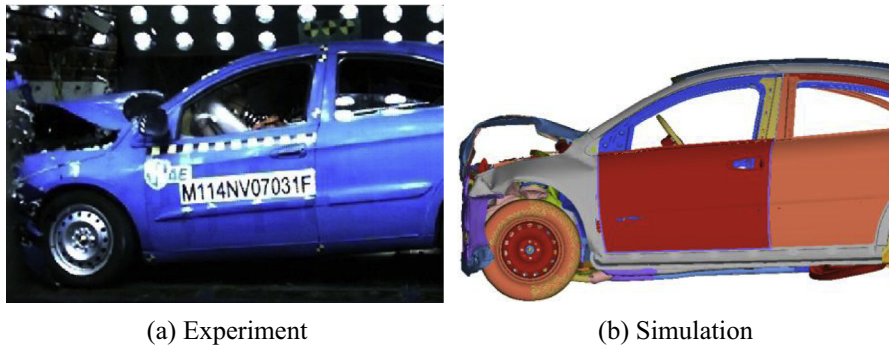
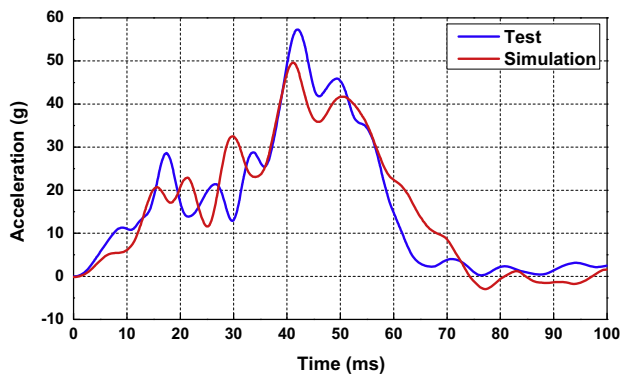
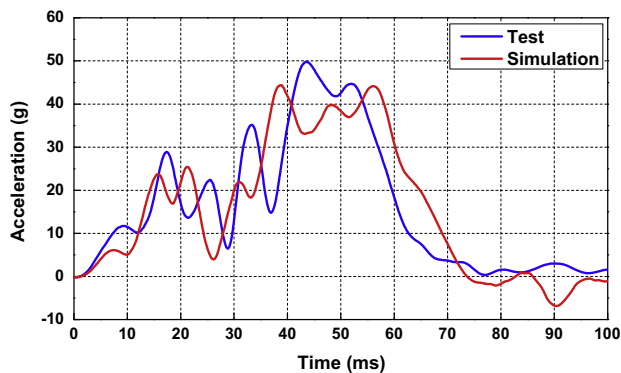


Fig. 8. Global deformation of baseline passenger car in frontal rigid wall impact at 50 km/h.



(a) Left side



(b) Right side

Fig. 9. B-pillar acceleration curve in the frontal rigid wall impact at 50 km/h.

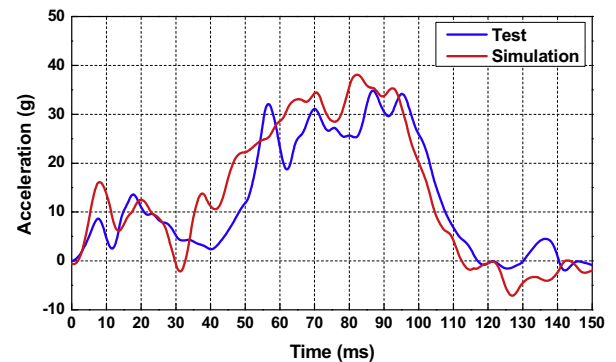


Fig. 11. B-pillar acceleration curve in ODB impact at 64 km/h.

curve of the test and simulation under the frontal offset impact, whose acceleration pulse of simulation is well correlated with that of offset impact test. The passenger compartment intrusion of simulation is also very similar to that of impact experiments in both the rigid wall impact and offset impact tests. Since the FE baseline model has the ability to replicate the crashing responses in real frontal impact tests, it is employed in the following analysis to explore the crashing performance of the foam-filled bumper system.

3. Finite element modeling of foam-filled bumper beam

In this study, a class of functionally graded foam was filled into the thin-walled structures of bumper beam as described in Section 2.2. The foam filler was modeled with standard solid elements and was divided into 80 layers along the length direction

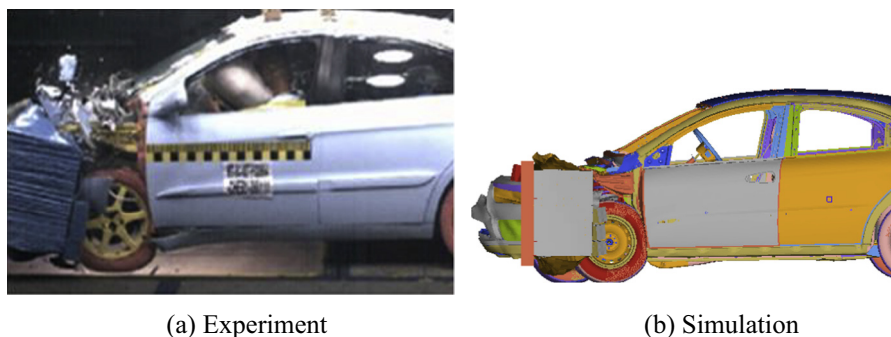


Fig. 10. Global deformation of baseline passenger car in ODB impact at 64 km/h.

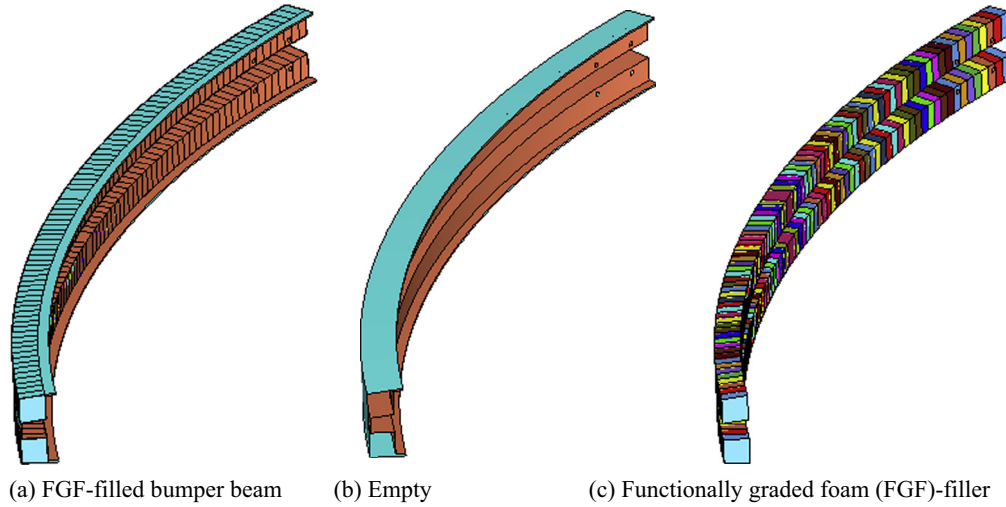


Fig. 12. FE models of hollow and foam filled bumper beam.

symmetrically (Fig. 12). Each layer was assigned a density value as defined in the gradient functions in Fig. 13 symmetrically. The corresponding material properties can be calculated based on the corresponding density value. The Belytschko–Tsay shell elements with five integration points through the thickness were employed to model the thin-wall structures and the foam elements were modeled using the 8-noded solid elements with the reduced integration technique. Stiffness-based hourglass control was employed to eliminate spurious zero-energy modes commonly arising due to use of the reduced integration elements. Element size of 5 mm was chosen for both the shell and solid elements after a convergence study.

Since the foam-filled bumper system consists of different materials and elements, different contact algorithms in LS-DYNA may need to be used. Automatic single surface contact was applied to the bumper walls, crash boxes and foam filler. The interface between the foam and bumper wall was modeled with a tied node to surface contact. Finally, automatic surface to surface contact was used between the impact surface of bumper and the rigid wall or ODB. The contacts were defined with static and dynamic coefficients of friction of 0.3 and 0.2, respectively.

It is assumed that the bumper beam is filled with FGF whose density varies along the length direction and is symmetrical about the mid section. The method to illustrate the density gradient of the functionally graded foam materials in thin-walled structures

is developed by Sun et al. [17] and other researchers [18,29,30]. The density gradient is defined in a power-law function as:

$$\begin{cases} \rho_f(y) = \rho_{f1} + (\rho_{f2} - \rho_{f1})\left(\frac{y}{l}\right)^m & \text{when } y < l \\ \rho_f(y) = \rho_{f1} + (\rho_{f2} - \rho_{f1})\left(\frac{2l-y}{l}\right)^m & \text{when } y > l \end{cases} \quad (6)$$

where ρ_{f1} and ρ_{f2} are the densities at the left/right ends and mid section, respectively, l is the half length of foam-filled bumper beam, y is the distance from left end, and m is the gradient parameter that governs the variation in foam density, and y/l is named as normalized distance, where 1 denotes mid section, 0 for the left end and 2 for the right end. For the case that the foam density increases along length from the left/right ends to mid surface, the gradient function changes from convex to concave, in which their value varies from less than 1 to greater than 1, as shown in Fig. 13. For the case that the foam density decreases along length from left/right end to mid surface, on the other hand, an opposite tendency can be formulated.

Then, mass of the FGF-filled bumper beam is calculated by the following formula:

$$\text{mass} = 3.217 \cdot t + 2 \cdot A \cdot \int_0^L \rho_{f1} + (\rho_{f2} - \rho_{f1})\left(\frac{y}{l}\right)^m dy \quad (\text{kg}) \quad (7)$$

where t is the thickness of thin walled steel bumper beam structures in millimeter, L is the half length of FGF-filled bumper beam of 0.593 m, A is cross section area of $2.123 \times 10^{-3} \text{ m}^2$. So,

$$\text{mass} = 3.217 \cdot t + 2.518 \times 10^{-3} \cdot \left(\rho_{f1} + \frac{\rho_{f2} - \rho_{f1}}{m+1} \right) \quad (\text{kg}) \quad (8)$$

For the uniform foam-filled bumper beam, above formula can be simplified as:

$$\text{mass} = 3.217 \cdot t + 2.518 \times 10^{-3} \cdot \rho_f \quad (\text{kg}) \quad (9)$$

where ρ_f is the density of the uniform foam filler in kg/m^3 .

Due to no constitutive model available for functionally graded foam material to date, the foam was divided into a number of layers along the bumper length direction. Each layer of foam filler was modeled with the homogeneous and isotropic foam model of material number 154 in LS-DYNA [31]. The following yield criterion of each uniform layer of foam material is assumed for this model:

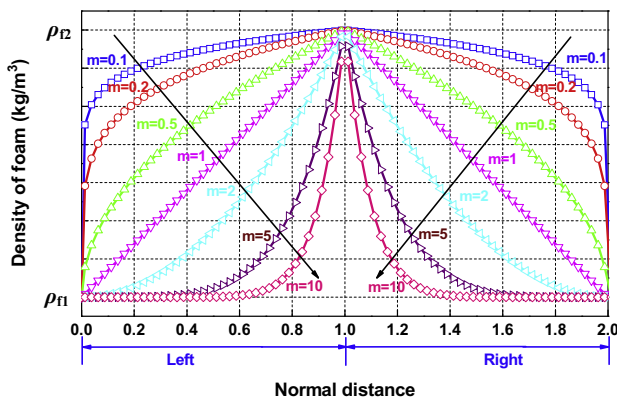


Fig. 13. Variation in density versus normalized distance (0 = left end, 1 = mid section of bump beam, 2 = left/right end).

Table 1
Material constants for aluminum foam.

	σ_p	α_2	$1/\beta$	γ	E_p
Material constants	C_0	0	0	0.22	0
	C_1	720	140	320	42
	n	2.33	0.45	4.66	1.42
Units	C_0	(MPa)	(MPa)	–	(MPa)
	C_1	(MPa)	(MPa)	–	(MPa)
	n	–	–	–	–

$$\phi = \hat{\sigma} - \sigma_y \leq 0 \quad (10)$$

where

$$\hat{\sigma}^2 = \frac{1}{[1 + (\alpha/3)^2]} [\sigma_e^2 + \alpha \sigma_m^2] \quad (11)$$

where σ_e is the effective von Mises stress, σ_m the mean stress and σ_y the yield strength. Parameter α defines the shape of the yield surface which is a function of the plastic coefficient of contraction, ν_p , as,

$$\alpha^2 = \frac{2(1 - 2\nu_p)}{9(1 + \nu_p)} \quad (12)$$

Thus the strain hardening rule is given in this material model as:

$$\sigma_y = \sigma_p + \gamma \frac{\hat{\epsilon}}{\epsilon_D} + \alpha_2 \ln \left(\frac{1}{1 - (\hat{\epsilon}/\epsilon_D)^\beta} \right) \quad (13)$$

where σ_p , α_2 , γ , ϵ_D and β are material parameters, and $\hat{\epsilon}$ the equivalent strain. Hardening rule is calibrated to a uniaxial compression test, and the compaction strain, ϵ_D , can be expressed as:

$$\epsilon_D = -\frac{9 + \alpha^2}{3\alpha^2} \ln \left(\frac{\rho_f}{\rho_{f0}} \right) \quad (14)$$

where ρ_f is the foam density of this layer and ρ_{f0} the density of the base material, which is 2.7 g/cm³ for aluminum.

The other material parameters σ_p , α_2 , γ , β and Young's modulus E_p can be also expressed as a function of the foam density ρ_f :

$$\left[\sigma_p, \alpha_2, \gamma, \frac{1}{\beta}, E_p \right] = C_0 + C_1 \left(\frac{\rho_f}{\rho_{f0}} \right)^n \quad (15)$$

where C_0 , C_1 and n are the material constants for material parameters σ_p , α_2 , γ , β and E_p and given in Table 1 [32,33].

Undoubtedly, it is better to validate all the established FEA models, including the model of aluminum foam. Unfortunately, there is no experimental data in house or in literature available for the specific bumper beam filled with aluminum foam. Alternatively, we validated the model by using the experiment of foam-filled square tube subjected to 3-point bending, which was done already in our previous study [34].

4. Parametric study

Parametric study is carried out here to quantify the effects of FGF-filled bumper beam parameters on crashworthiness. The selected parameters are the gradient exponent m , end foam densities ρ_{f1} and ρ_{f2} , and wall thickness t ; the crashworthiness criteria are energy absorption EA, specific energy absorption SEA, peak force F_{max} and crash force efficiency CFE.

4.1. Effect of density gradient

In order to explore the effect of density gradient on crashworthiness and compare the energy absorbing ability of the FGF with UF filled structure, a group of FGF and UF bumper beams with the same mass were analyzed. In each case, the wall thickness of bumper beam is set to 1.0 mm, and the end densities ρ_{f1} and ρ_{f2} of all FGF-filled bumper beams are 50 kg/m³ and 800 kg/m³, respectively. The FGF-filled bumper beams with different exponent m (0, 0.2, 0.4, 0.6, 0.8, 1, 2, 4, 6, 8 and 10) are considered here. Corresponding foam density for the uniform foam is calculated under the same mass as the graded foam with different exponent m . For this purpose, the foam density ρ_U of the uniform foam is the average foam density of corresponding FGF-filler as expressed in term of m as:

$$\rho_U = \rho_{f1} + \frac{\rho_{f2} - \rho_{f1}}{m + 1} \quad (16)$$

Obviously, the foam densities of UF-filled bumper beams monotonously increase with decreasing m . For example, the foam density ρ_U is 118 kg/m³ for $m = 10$, 425 kg/m³ for $m = 1$, and reaching the highest density 800 kg/m³ when $m = 0$.

From Fig. 14, it is clear that exponent m has great influence on EA of FGF and UF filled bumper beam. FGF beam absorbs more energy than UF beam over the entire range of gradient. EA of FGF-filled bumper beam increases with the increase of m when m less than 0.4, but decreases when m greater than 0.4. EA of UF-filled bumper beam decreases with the increase of m except the range of $0.4 \leq m \leq 0.8$.

From Fig. 15, SEA of FGF-filled beam increases with the increase of m when m below 4.0, whereas decreases when m is above 4.0. SEA of UF-filled beam increases with the increase in m when m is

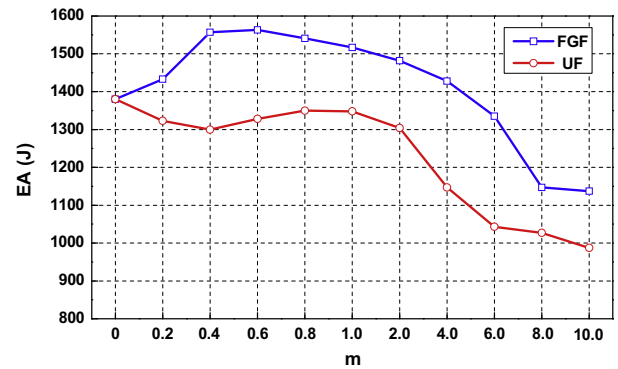


Fig. 14. Influence of foam density gradient m on energy absorption EA.

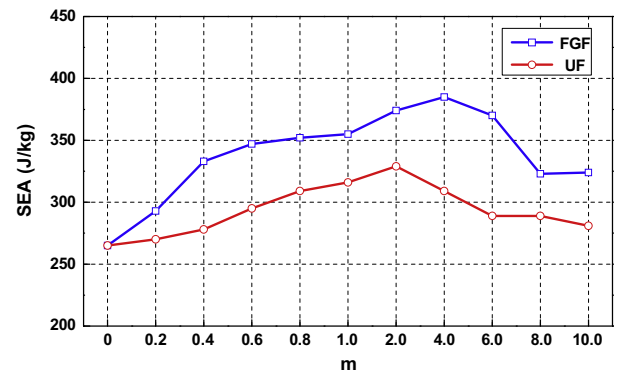


Fig. 15. Influence of foam density gradient m on SEA.

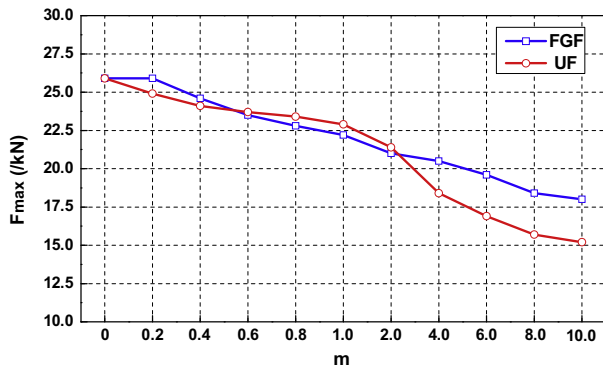
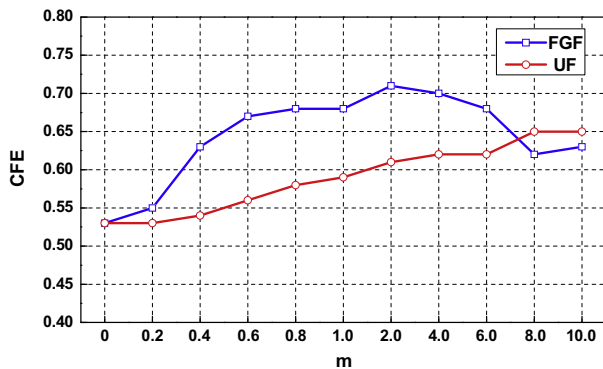
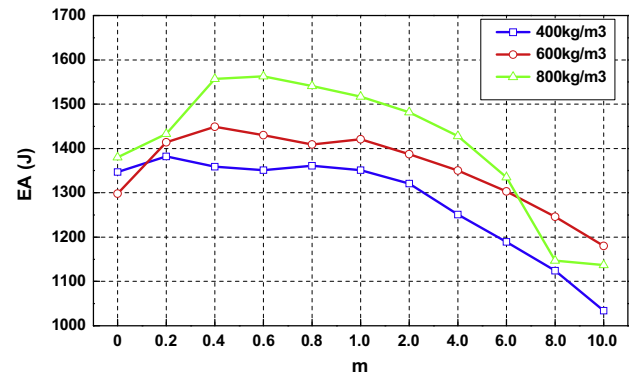
Fig. 16. Influence of foam density gradient m on peak force.Fig. 17. Influence of foam density gradient m on CFE.

Fig. 18. Influence of density range on EA.

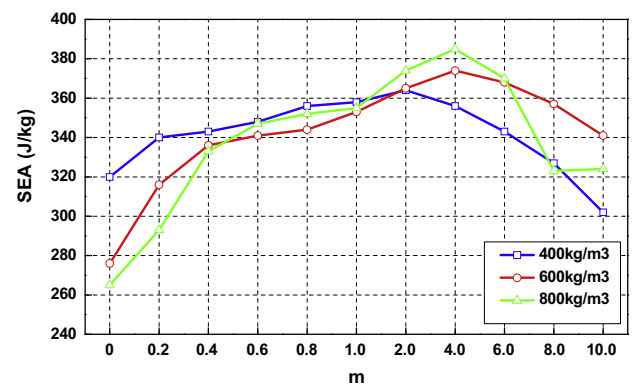


Fig. 19. Influence of density range on SEA.

below 2.0, whereas decreases when m is above 2.0. It is clear that SEA of the FGF-filled beam is higher than that of the corresponding UF-filled bumper beam over the entire range considered. The results plotted in Figs. 14 and 15 clearly indicated that energy absorbing capacity of the FGF-filled beam is superior to the UF-filled beam.

Fig. 16 shows the influence of m on the peak impact force of FGF and UF filled bumper beam. The peak forces both decrease with the increase in m . Peak force of FGF-filled bumper beam is similar to that of corresponding UF-filled bumper beam when m is less than 2.0, whereas is above UF-filled bumper beam when m is greater than 2.0.

Fig. 17 shows the influence of m on CFE of FGF and UF beam. CFE of FGF beam increases with the increase in m when m is less than 2.0. CFE of UF increases with the increase in m almost in the whole range. It is clear CFE of FGF beam is larger than the UF beam in the most of the range, indicating that FGF filler is more ideal than UF filler in the bump beam structure.

From the above analysis, the crashworthiness of FGF-filled is better than that of UF-filled bumper beam, potentially being more advantageous in improving crashing behaviors for the passenger car.

4.2. Effect of density range

To explore the effect of foam density range, three different foam densities ρ_{f2} of 400 kg/m³, 600 kg/m³ and 800 kg/m³, have been investigated, while foam density ρ_{f1} and wall thickness are remained as 50 kg/m³ and 1.0 mm, respectively.

Figs. 18–21 show the relationship of foam density range with EA, SEA, F_{max} and CFE. It is noted that foam density has significant influence on crashworthiness of FGF beam, especially EA and

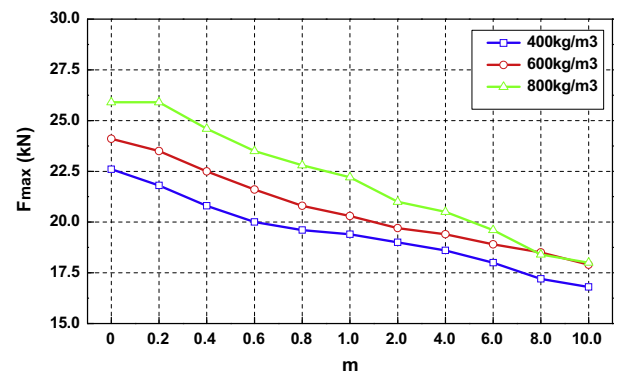


Fig. 20. Influence of density range on peak force.

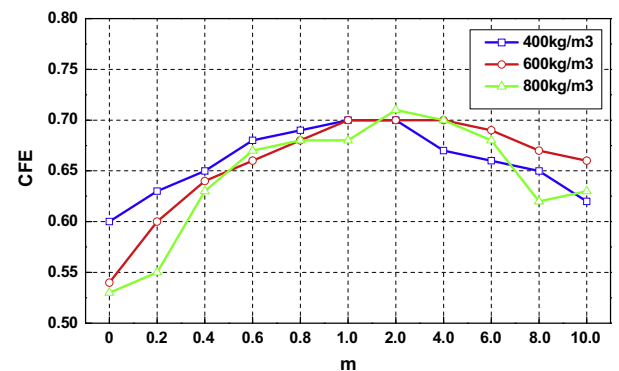


Fig. 21. Influence of density range on CFE.

F_{max} . Fig. 18 shows that a higher ρ_{f2} value of 800 kg/m³ results in higher energy absorption when m is less than 6.5, whereas intermediate ρ_{f2} value of 600 kg/m³ leads to higher energy absorption when m is larger than 6.5.

The relationship between foam density and SEA is fairly complicated, seen in these three curves of different foam density ρ_{f2} intersecting each other (Fig. 19). SEA first increases and then decreases with the increase in m , achieving a peak value between $m = 2.0$ and $m = 6.0$ for different foam densities ρ_{f2} .

In Fig. 20, the peak crashing force F_{max} increases with the increase in foam density ρ_{f2} and the decrease of exponent m . However, a higher foam density ρ_{f2} does not lead to a higher crash force efficiency CFE as shown in Fig. 21.

4.3. Effect of wall thickness

To explore the influence of wall thickness of bumper beam on crashworthiness, the responses of four groups of FGF-filled bumper beam with different wall thickness were compared. Foam density ρ_{f1} and ρ_{f2} maintain the same values as 50 kg/m³ and 800 kg/m³. In each group, the wall thickness of bumper beam is set to 0.8 mm, 1.0 mm, 1.2 mm and 1.4 mm respectively. Figs. 22–25 show the relationship between crashworthiness criteria (EA, SEA, F_{max} and CFE) and wall thickness. It is clear that larger wall thickness means more energy absorption (higher EA), but it does not lead to a higher SEA. From Fig. 23, it can be seen that exponent m of 4.0 and wall thickness of 1.0 mm can result in a high SEA value of 385 J/kg.

As shown in Fig. 24, peak force decreases with the increase of exponent m and decrease of wall thickness. From Fig. 25, the influence of wall thickness on crash force efficiency (CFE) is complicated. Exponent of 1.0 and wall thickness of 0.8 mm can lead to a peak CFE value of 0.716.

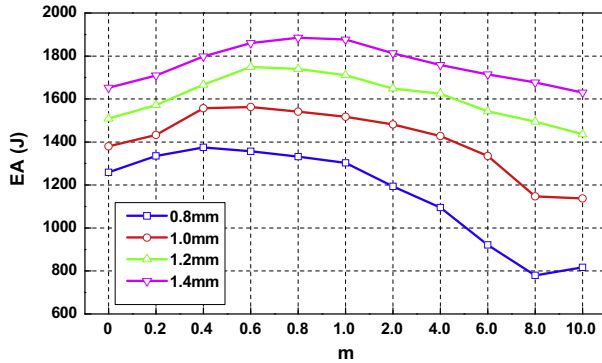


Fig. 22. Influence of wall thickness on EA.

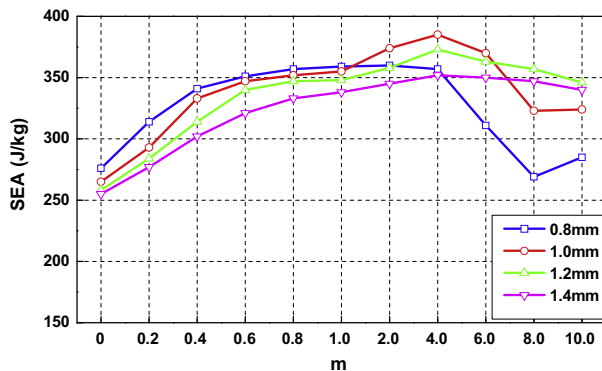


Fig. 23. Influence of wall thickness on SEA.

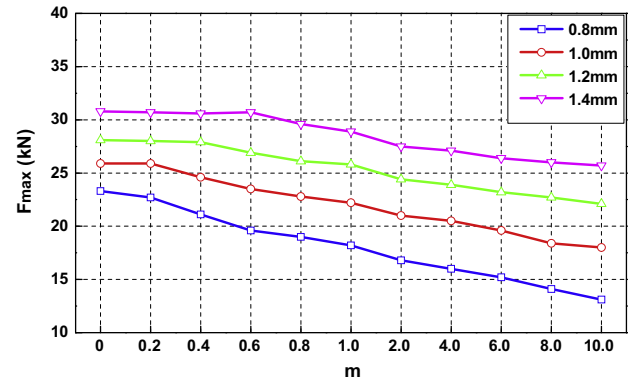


Fig. 24. Influence of wall thickness on peak force.

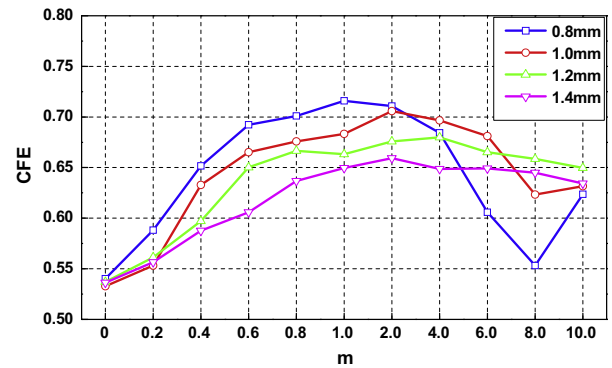


Fig. 25. Influence of wall thickness on CFE.

These above design parameters have been shown the significant effect on crashworthiness. It is thus necessary to seek the optimal design of FGF-filled bumper beam next step.

5. Multiobjective optimization for crashworthiness criteria

5.1. Optimization formulation

For bumper beam, the peak crash force F_{max} is an important indicator for the safety of the occupants, which should be minimized. As an energy absorber, the structure is expected to absorb as much impact energy as possible per unit mass. Thus, SEA should be an objective function and be maximized. Thus, we formulate the multiobjective optimization problems for FGF filled bumpers in Eq. (17), to simultaneously enhance these two design criteria. Four design variables (t , ρ_{f1} , ρ_{f2} , m) were selected for the optimization problem.

$$\begin{cases} \text{Minimize} & [F_{max}(t, \rho_{f1}, \rho_{f2}, m), -SEA(t, \rho_{f1}, \rho_{f2}, m)] \\ \text{s.t.} & 0.8 \text{ mm} \leq t \leq 1.5 \text{ mm} \\ & 50 \text{ kg/m}^3 \leq \rho_{f1} \leq 400 \text{ kg/m}^3 \\ & 400 \text{ kg/m}^3 \leq \rho_{f2} \leq 800 \text{ kg/m}^3 \\ & 0.1 \leq m \leq 10 \end{cases} \quad (17)$$

For comparison, the multiobjective optimization problem for UF filled and hollow bumper beam is also defined in Eqs. (18) and (19) respectively, where the wall thickness (t) and foam density (ρ_f) are taken as design variables.

$$\begin{cases} \text{Minimize} & [F_{max}(t, \rho_f), -SEA(t, \rho_f)] \\ \text{s.t.} & 0.8 \text{ mm} \leq t \leq 1.5 \text{ mm} \\ & 50 \text{ kg/m}^3 \leq \rho_f \leq 800 \text{ kg/m}^3 \end{cases} \quad (18)$$

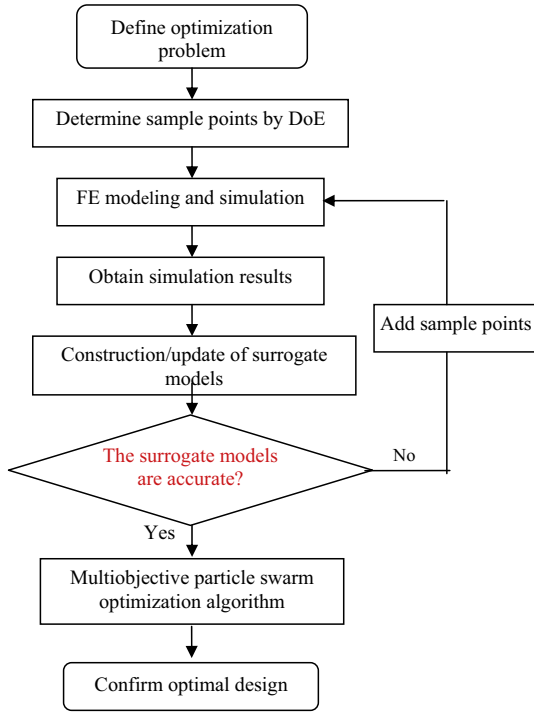


Fig. 26. Flowchart of design optimization.

$$\begin{cases} \text{Minimize} & [F_{\max}(t), -SEA(t)] \\ \text{s.t.} & 0.8 \text{ mm} \leq t \leq 1.5 \text{ mm} \end{cases} \quad (19)$$

The general procedure of the implementation of the multiobjective optimization (MDO) in crashworthiness is depicted in Fig. 26.

5.2. Surrogate establishment and accuracy assessment

Since the crashworthiness problem of FGF-filled bumper structure is highly nonlinear and complicated, direct coupling of optimization algorithm with simulation model may not be efficient (if possible) as iterative analyses during optimization is required to be involved. As an alternative, the metamodeling or surrogate modeling techniques have proven effective to replace full simulations for the optimization [1,35–37]. The surrogate model can provide an approximate functional relationship to relate design variables to specific objective with a moderate number of full computational analyses. In this regard, the Kriging method has exhibited a fairly good accuracy for highly nonlinear design problems [38,39] and will be employed to construct the surrogate models for crashworthiness objectives in this paper.

The Kriging model was originally developed for mining and geo-statistical applications involving spatially and temporally correlated data [40]. The Kriging model assumes the deterministic response of a system to be a stochastic process function $y(\mathbf{x})$, consisting of a regression model and a stochastic error:

$$y(\mathbf{x}) = \mathbf{f}(\mathbf{x})^T \boldsymbol{\beta} + z(\mathbf{x}) \quad (20)$$

where $\boldsymbol{\beta}$ is the column vector of regression parameters, $\boldsymbol{\beta} = [\beta_1, \beta_2, \dots, \beta_p]^T$; $\mathbf{f}(\mathbf{x})$ is the column vector of basis functions, $\mathbf{f}(\mathbf{x}) = [f_1(\mathbf{x}), f_2(\mathbf{x}), \dots, f_p(\mathbf{x})]^T$; p denotes the number of basis functions; $z(\mathbf{x})$ represents a stochastic parameter with zero mean, variance σ^2 , and nonzero covariance.

After surrogate models are established, their accuracy should be assessed. To assess the fitting accuracy of surrogate models, such metrics as R -square (R^2), maximum relative error (e_{\max}) and average relative error (e_{avg}) are adopted as follows:

$$R^2 = 1 - \frac{\sum_{i=1}^q (y_i - \hat{y}_i)^2}{\sum_{i=1}^q (y_i - \bar{y})^2} \quad (21)$$

$$e_{\max} = \max_{i \in \{1, \dots, q\}} \left(\frac{|y_i - \hat{y}_i|}{|y_i|} \right) \quad (22)$$

$$e_{\text{avg}} = \frac{1}{q} \sum_{i=1}^q \frac{|y_i - \hat{y}_i|}{|y_i|} \quad (23)$$

where y_i denotes the exact function value for confirmation point i , \hat{y}_i is the corresponding surrogate value, \bar{y} is the mean of y_i , q is the number of the confirmation sampling points. It can be seen that a larger value of R^2 is preferred, which indicates a higher accuracy for overall performance in the design space. On the other hand, smaller values of e_{\max} and e_{avg} are preferred, which qualifies the relative errors at the checking points.

Table 2 summarizes the results of accuracy assessment of the surrogate models. Clearly, the values of R^2 are all close to 1 and the values of e_{\max} and e_{avg} are within 6%, indicating that the Kriging models are adequately accurate to replace the high-fidelity finite element analyses.

5.3. Multiobjective particle swarm optimization (MOPSO) algorithm

To address the optimization problem defined in Eqs. (17)–(19), multiobjective particle swarm optimization (MOPSO) algorithm is implemented. Particle swarm optimization (PSO) algorithm is inspired by the choreography of a bird flock [41]. As an extended version to PSO, MOPSO is characterized by fast convergence and well-distributed Pareto frontier compared with other multiobjective optimization algorithms such as NSGA-II, PEAS and microGA [42]. MOPSO has been employed successfully to solve the design problems of sheet metal forming [43] and crashworthiness for functionally graded foam-filled structures [17]. In this paper, it is utilized to handle the optimization problem for FGF-filled bumper structure. The parameters to solve the multiobjective optimization problems are given in Table 3.

5.4. Multiobjective optimization results for bumper beam component

Fig. 27 depicts the Pareto frontiers of the multiobjective optimizations for the hollow, FGF and UF bumper beam. Overall, the Pareto optimal frontier provides designers with a set of solutions over the Pareto space for design selection. Specifically, if the designers pay more attention to SEA, the solutions at the

Table 2
Accuracy assessment of Kriging models.

			R^2	e_{max} (%)	e_{avg} (%)
Hollow bumper	SEA		0.9859	1.46	0.82
	F_{max}		0.9994	0.78	0.52
UF bumper	SEA		0.9822	4.05	1.61
	F_{max}		0.9448	5.43	2.76
FGF bumper	$0 \leq m < 1$	SEA	0.9666	4.83	1.85
		F_{max}	0.9842	2.91	1.57
	$1 \leq m \leq 10$	SEA	0.9510	5.60	2.66
		F_{max}	0.9651	5.48	2.05

Table 3
Parameters for implementing MOPSO procedure.

MOPSO parameter name	Value
Population size	100
Number of generations	100
External archive size	100
Inertial weight	0.73
Personal learning coefficient	1.50
Global learning coefficient	1.50

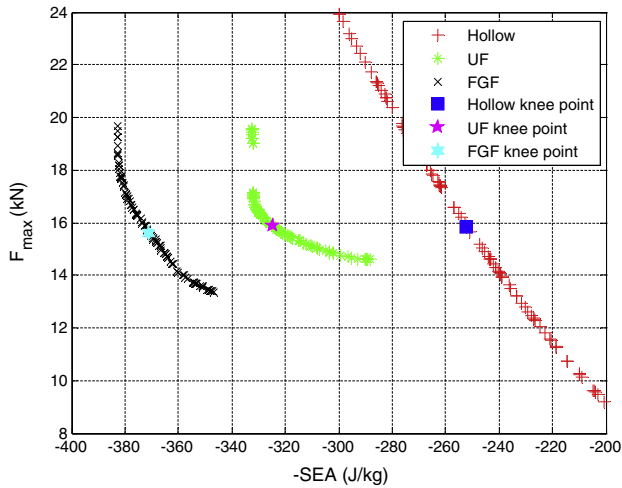


Fig. 27. Pareto frontiers of the multiobjective optimizations for the FGF and UF bumper beam.

bottom right corner should be considered. Whereas if the designers wish to emphasize F_{max} , the solutions at the top left corner should be considered.

Interestingly, when the bumper bar is filled with foams, the Pareto frontier moves left in the objective space, representing that the SEA can be improved significantly under the same F_{max} . Furthermore, replacing UF by FGF enable the bumper to yield more

promising designs with a much larger SEA under the same F_{max} . Particularly, even the lowest SEA value of the FGF solutions in the Pareto frontier is larger than the highest SEA value of the UF solution.

To select an overall optimal point from the Pareto set, the minimum distance selection method (TMDSM) is usually adopted, namely knee point [2]. The knee point in a Pareto frontier usually signifies a good trade-off between the competing objectives, and in most cases it is found to have the shortest distance (relative to other Pareto points) to the utopia point. In this sense, such a design point generally provides an overall optimum in the objective space. Since F_{max} and SEA have different orders of magnitude, they are normalized to the range from 0 to 1 prior to using TMDSM. The

Table 4

Knee points of optimization problems and crashworthiness results.

		Variables				Objectives	
		t (mm)	$\rho_f(\rho_f)$ (kg/m ³)	ρ_{p2} (kg/m ³)	m	SEA (J/kg)	F_{max} (kN)
Hollow	Kriging	1.17	–	–	–	252.09	15.85
	FEA					251.34	15.80
	Error					0.30%	0.33%
UF	Kriging	0.80	235.04	–	–	324.76	15.88
	FEA					322.80	15.73
	Error					–0.60%	–0.94%
FGF	Kriging	0.80	107.44	789.30	8.06	371.09	15.61
	FEA					360.44	15.84
	Error					–2.87%	1.47%

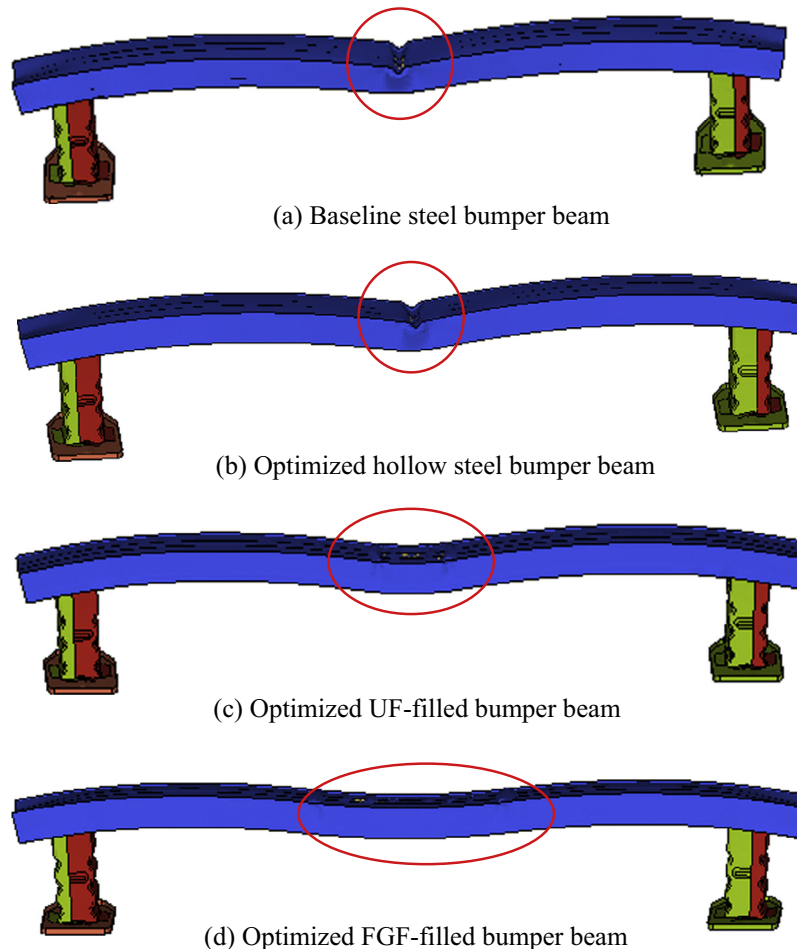


Fig. 28. Deformation mode of hollow and FGF-filled bumper beam.

knee points of these three optimizations and their results are summarized in Table 4.

To understand the crashing behaviors, the deformation modes of hollow steel baseline bumper beam, optimized UF and FGF-filled bumper beams at the knee points are compared here. As shown in Fig. 28, the deformation of hollow steel beam is mainly localized in the impactor contact area both in baseline model and optimized hollow model. Whereas the deformation of the optimized UF-filled bumper beam does not concentrate on this area and the deformation area of FGF-filled bumper beam is even wider than the UF counterpart. From this perspective, the FGF-filled bumper deforms in a most preferable way of these bumpers.

The impact force histories of the baseline hollow bumper beam, optimized UF and FGF-filled bumper beams at the knee point solutions are shown in Fig. 29. The impact force of the baseline model reaches a peak value of 14.0 kN at time of

31.5 ms and then decreases dramatically due to the local collapse of the hollow bumper beam. For the optimized hollow bumper beam, the shape of impact force curve is similar to baseline model because of only wall thickness is changed, while the peak force is 15.80 kN occurred at 34.6 ms. With broader range of material deformation, the impact force of the UF-filled bumper beam reaches a higher peak of 15.73 kN at time of 49.2 ms. The impact force of FGF-filled bumper beam achieves the highest peak of 15.84 kN at time of 49.2 ms. Importantly, the FGF component maintains such a high force level over 14 kN much longer than the UF and baseline counterparts. At the same time, the mass of optimized FGF-filled component is 3.03 kg, which is less than the UF-filled of 3.16 kg, hollow base model of 3.54 kg and optimized hollow model of 3.76 kg.

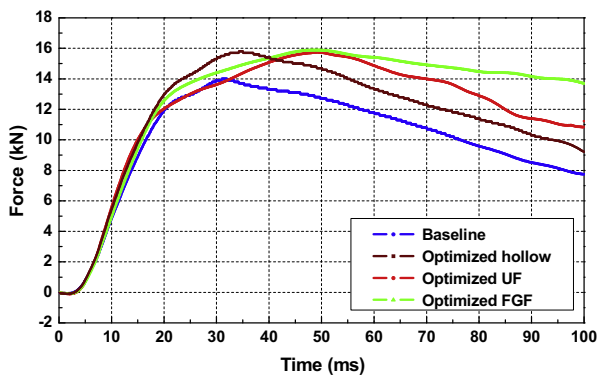


Fig. 29. Crashing force histories of hollow and foam-filled bumper beams.

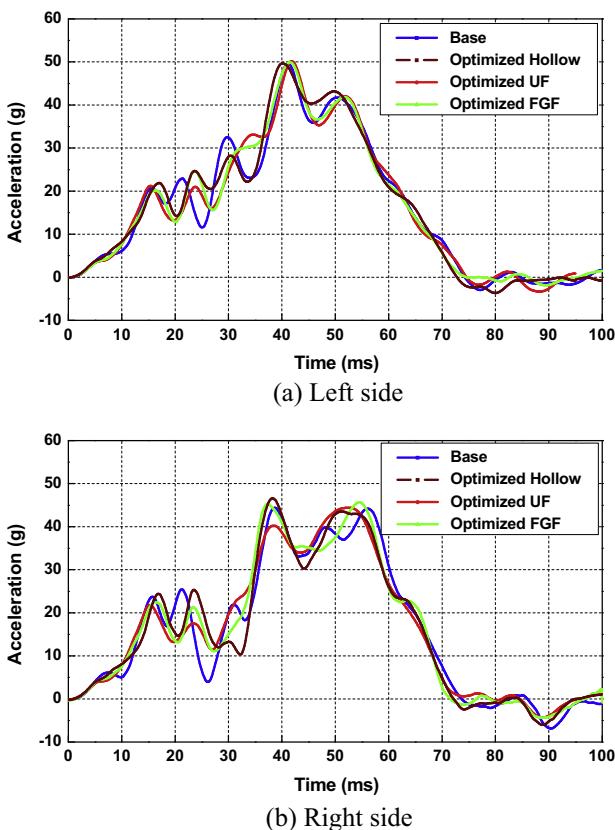


Fig. 30. Compare of B-pillar acceleration curves of passenger car models with the optimized and baseline bumper model in frontal rigid wall impact at 50 km/h.

5.5. Crashworthiness of optimized foam-filled bumper beam in a passenger car model

The optimized hollow, UF-filled and FGF-filled bumper beam at the knee point solutions were applied in the original passenger car model to investigate their performance on impact responses in the whole car system.

Figs. 30 and 32 plot the B-pillar acceleration curves of passenger car with the optimized and baseline bumper model under the frontal rigid wall impact and ODB offset impact, respectively. It can be observed that the B-pillar acceleration curves of passenger car with optimized foam-filled and hollow bumper are fairly similar to that of the baseline bumper. As summarized in Table 5, the peak acceleration values of the passenger car with optimized foam-filled bumper are slightly higher than baseline model both in the frontal rigid wall impact and offset ODB impact. And the pulse waveform efficiencies of passenger car decreased when the optimized bumper model was adopted, as in Table 5.

Figs. 31 and 33 plot the firewall intrusion contour of the passenger car with the optimized and baseline bumper beams in the frontal rigid wall impact and offset ODB impact. The maximum intrusion of firewall decreases when using the optimized UF or FGF-filled bumper beam in the both impacts. For the baseline model, the maximum firewall intrusion values are 132 mm and 171 mm in frontal rigid wall and offset ODB impacts respectively, while for passenger car model with optimized hollow bumper beam, the values are 123 mm and 174 mm. For passenger car model with the optimized UF-filled bumper beam, the maximum firewall intrusion values are 123 mm and 167 mm. And for passenger car with the optimized FGF-filled bumper beam, the maximum firewall intrusion values are 127 mm and 169 mm.

A-pillar displacement, steering column intrusion, pedals intrusion of passenger car with the optimized and baseline bumper beams are listed in Table 5. For the 50 km/h frontal rigid wall impact, the impact pulse parameters slightly decreased when using the optimized foam-filled bumper beam while the intrusion remained almost unchanged. For the 64 km/h offset ODB impact, the passenger car with the optimized FGF-filled beam led to a slightly higher acceleration but relatively lower pedal intrusion.

From the above analyses, the acceleration criteria seemed to be slightly worsened while intrusion criteria were improved when the optimized FGF-filled bumper beam was adopted in the passenger car model. In addition, the optimized FGF-filled bumper beam can reduce the weight of 14.4% relative to the base bumper beam model without sacrificing the crashworthiness of the passenger car.

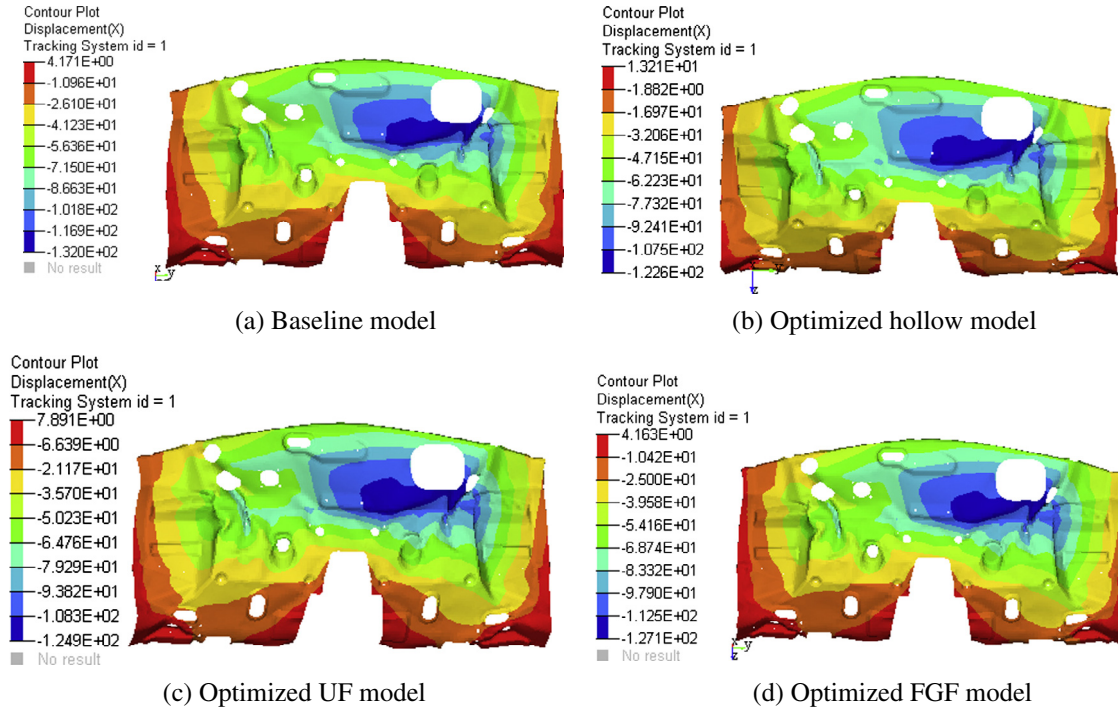


Fig. 31. Comparison of car firewall intrusion contour of the passenger car models with the optimized and baseline bumper model in frontal rigid wall impact at 50 km/h.

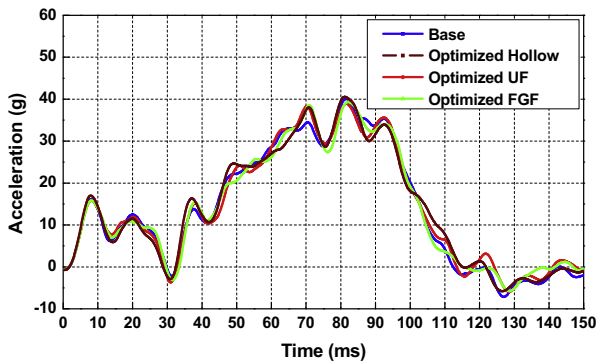


Fig. 32. Compare of B-pillar acceleration curves of the passenger car models with the optimized and baseline bumper model in offset ODB impact at 64 km/h.

Table 5

Simulation results of passenger car with the optimized UF/FGF-filled and baseline bumper beams.

Crashworthiness criteria		Rigid wall impact at 50 km/h				ODB impact at 64 km/h			
		Base model	Optimized hollow bumper beam	Optimized UF bumper beam	Optimized FGF bumper beam	Base model	Optimized hollow bumper beam	Optimized UF bumper beam	Optimized FGF bumper beam
Peak acceleration A_p (g)	Left	49.6	49.7	50.2	49.9	38.1	40.6	38.9	39.4
	Right	44.4	46.6	45.2	45.7	–	–	–	–
Pulse waveform efficiency (η)	Left	37.69%	37.60%	37.49%	37.67%	39.12%	36.78%	38.36%	37.65%
	Right	40.33%	39.05%	39.86%	39.62%	–	–	–	–
A-pillar displacement (mm)	Left	14	14	7	6	16	16	16	17
	Right	23	24	26	25	8	9	9	9
Steering column intrusion (mm)	x-axis	23	17	19	14	40	32	28	40
	z-axis	71	81	90	69	80	81	80	77
Acceleration pedal intrusion (mm)	x-axis	32	30	29	31	105	102	94	90
	z-axis	13	10	10	12	29	23	20	22
Brake pedal intrusion (mm)	x-axis	38	36	35	34	114	107	108	101
	z-axis	12	14	7	9	31	24	21	21
Switch pedal intrusion (mm)	x-axis	36	37	39	36	160	153	152	148
	z-axis	12	14	12	7	56	49	46	47
Firewall intrusion (mm)	x-axis	132	123	123	127	171	174	167	169

6. Conclusion

A FGF-filled bumper beam system was studied in this paper, aimed to improve the energy absorption under impact. A numerical FGF-filled bumper beam model was built with explicit finite element code LS-DYNA. Parametric study was conducted to explore the effects of FGF-filled bumper beam parameters on crashworthiness in comparison with the UF-filled bumper beams. It was found that the FGF-filled bumper beam allowed absorbing more impact energy than the UF-filled with the same weight. Density gradient m , density range (ρ_{f1} and ρ_{f2}), and wall thickness t have significant effects on EA , SEA , F_{max} , and CFE .

The Kriging surrogate modeling technique and multiobjective particle optimization (MOPSO) algorithm were then implemented to optimize the FGF-filled bumper beam by minimizing F_{max} and

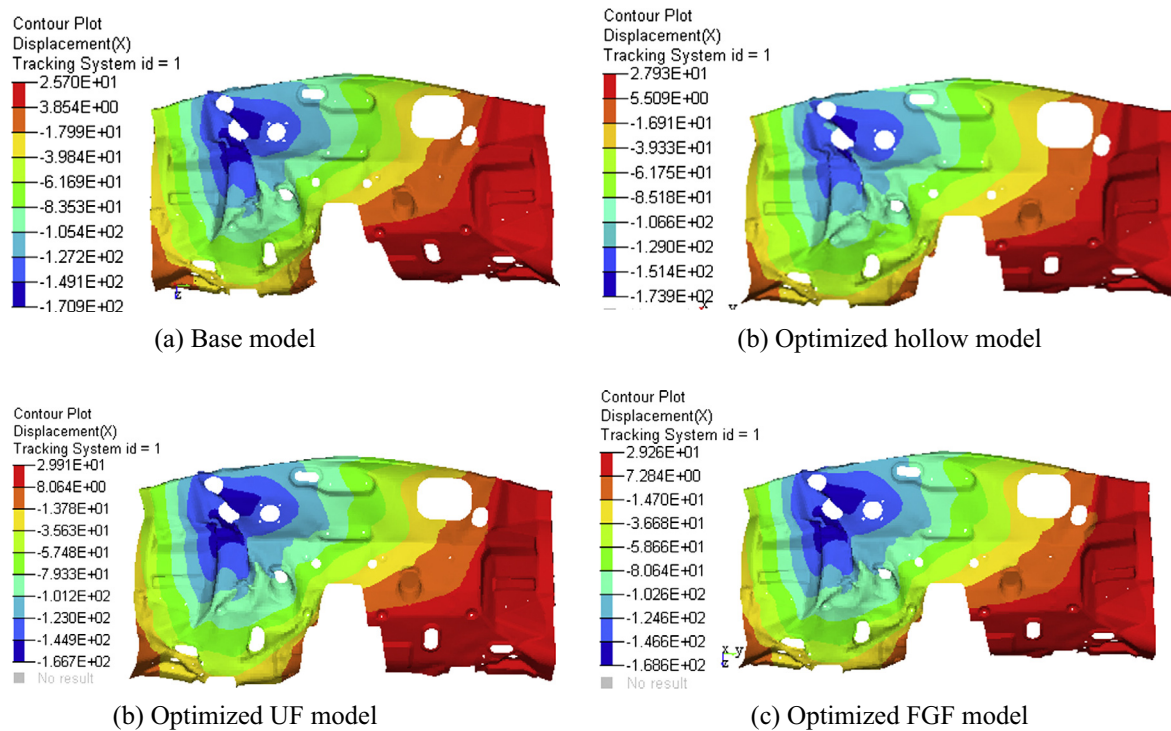


Fig. 33. Comparison of car firewall intrusion contour of passenger car models with the optimized and baseline bumper model in offset ODB impact at 64 km/h.

maximizing SEA simultaneously. Pareto optimum results showed that the FGF-filled bumper had a more ideal deformation behavior and absorbed more energy than the hollow baseline and UF-filled counterparts.

Finally, the optimized UF-filled and FGF-filled bumper beam at the knee point solutions were introduced in a validated passenger car model to compare their performance in the frontal rigid wall impact at 50 km/h and offset ODB impact at 64 km/h. The simulation results showed that the FGF-filled bumper beam can achieve a weight reduction of 14.4% compared with the original bumper beam model while maintaining the same level of crashworthiness. As a preliminary study, this paper has already proven that FGF structure could be a potential energy absorber in automobile industry. However, other factors such as fracture and property variation in foam materials should be taken into account in a more realistic way, which will be part of our future work.

Acknowledgements

This work is supported by The Young Teacher Development Plan of Hunan University, The National Natural Science Foundation of China (51475154, 11202072), The Science Fund of State Key Laboratory of Advanced Design and Manufacturing for Vehicle Body in China (No. 61075004), the Doctoral Fund of Ministry of Education of China (20120161120005).

References

- [1] Yang RJ, Wang N, Tho CH, Bobineau JP. Metamodeling development for vehicle frontal impact simulation. *J Mech Des* 2005;127(5):1014–20.
- [2] Sun GY, Li GY, Zhou SW, Li HZ, Hou SJ, Li Q. Crashworthiness design of vehicle by using multiobjective robust optimization. *Struct Multidisc Optim* 2011;44(1):99–110.
- [3] Kecman D. Bending collapse of rectangular and square section tubes. *Int J Mech Sci* 1983;25(9–10):623–36.
- [4] Wierzbicki T, Recke L, Abramowicz W, Gholami T, Huang J. Stress profiles in thin-walled prismatic columns subjected to crush loading-II. Bending. *Comput Struct* 1994;51(6):625–41.
- [5] Liu YC, Day ML. Bending collapse of thin-walled beams with channel cross-section. *Int J Crashworthiness* 2006;11(3):251–62.
- [6] Guo LW, Yu JL. Dynamic bending response of double cylindrical tubes-filled with aluminum foam. *Int J Impact Eng* 2011;38(2–3):85–94.
- [7] Reddy TY, Wall RJ. Axial compression of foam-filled thin-walled circular tubes. *Int J Impact Eng* 1988;7(2):151–66.
- [8] Seitzberger M, Rammerstorfer FG, Degischer HP, Gradinger R. Crushing of axially compressed steel tubes filled with aluminum foam. *Acta Mech* 1997;125(1–4):93–105.
- [9] Banhart J. Manufacture characterisation and application of cellular metals and metal foams. *Prog Mater Sci* 2001;46(6):559–632.
- [10] Yu JL, Wang EH, Li JR, Zheng ZJ. Static and low-velocity impact behavior of sandwich beams with closed-cell aluminum-foam core in three-point bending. *Int J Impact Eng* 2008;35(8):885–94.
- [11] Santosa S, Wierzbicki T. Effect of a ultralight metal filler on the bending collapse behavior of thin-walled prismatic columns. *Int J Mech Sci* 1999;41(8):995–1019.
- [12] Chen W, Wierzbicki T, Santosa S. Bending collapse of thin-walled beams with ultralight filler: numerical simulation and weight optimization. *Acta Mech* 2002;153(3–4):183–206.
- [13] Zarei HR, Kröger M. Bending behavior of empty and foam-filled beams: structural optimization. *Int J Impact Eng* 2008;35(6):521–9.
- [14] Duarte I, Vesenjak M, Opara LK. Dynamic and quasi-static bending behavior of thin-walled aluminum tubes-filled with aluminum foam. *Compos Struct* 2014;109:48–56.
- [15] Gupta N, Ricci W. Comparison of compressive properties of layered syntactic foams having gradient in microballoon volume fraction and wall thickness. *Mater Sci Eng A* 2006;427(1–2):331–42.
- [16] Gupta N. A functionally graded syntactic foam material for high energy absorption under compression. *Mater Lett* 2007;61(4–5):979–82.
- [17] Sun GY, Li GY, Hou SJ, Zhou SW, Li W, Li Q. Crashworthiness design for functionally graded foam-filled thin-walled structures. *Mater Sci Eng A* 2010;527(7–8):1911–9.
- [18] Attia MS, Meguid SA, Nouraei H. Nonlinear finite element analysis of the crush behaviour of functionally graded foam-filled columns. *Finite Elem Anal Des* 2012;61:50–9.
- [19] Yin HF, Wen GL, Hou SJ, Qing QX. Multiobjective crashworthiness optimization of functionally lateral graded foam-filled tubes. *Mater Des* 2013;44:414–28.
- [20] Yin HF, Wen GL, Fang HB, Qing QX, Kong XZ, Xiao JR, et al. Multiobjective crashworthiness optimization design of functionally graded foam-filled tapered tube based on dynamic ensemble metamodel. *Mater Des* 2014;55:747–57.
- [21] Kim HS. New extruded multi-cell aluminum profile for maximum crash energy absorption and weight efficiency. *Thin-Wall Struct* 2002;40(4):311–27.
- [22] Zarei HR, Kröger M. Crashworthiness optimization of empty and filled aluminum crash boxes. *Int J Crashworthiness* 2007;12(3):255–64.

- [23] Tang ZL, Liu ST, Zhang ZH. Analysis of energy absorption characteristics of cylindrical multi-cell columns. *Thin-Wall Struct* 2013;62:75–84.
- [24] Chou CC. Vehicle crashworthiness and occupant protection – fundamental principles for vehicle/occupant systems analysis. American Iron and Steel Institute; 2004. <http://www.autosteel.org/safety_book/index.htm> [accessed 08.05.14].
- [25] Fu Y, Abramowski E. Robust design for occupant restraint system. SAE technical paper; 2005.
- [26] Kawabe Y, Kondo T, Hirayama S, Obayashi K, Okabe T. Multi-parameter, multi-objective optimization of injury indexes of vehicle crash models. SAE technical paper; 2005.
- [27] Mizuno K, Wani K, Yonezawa H. Vehicle crashworthiness in full and offset frontal impact tests. *JSAE Rev* 2003;24(2):173–81.
- [28] Siegel JH, Mason-Gonzalez S, Dischinger P, Cushing B, Read K, Robinson R, et al. Safety belt restraints and compartment intrusions in frontal and lateral motor vehicle crashes: mechanisms of injuries, complications, and acute care costs. *J Trauma* 1993;34(5):736–59.
- [29] Brothers AH, Dunand DC. Density-graded cellular aluminum. *Adv Eng Mater* 2006;8(9):805–9.
- [30] Henderson B, Whitty JPM, Myler P, Chirwa C. Crash performance of cellular foams with reduced relative density part 2: rib deletion. *Int J Crashworthiness* 2007;12(6):689–98.
- [31] Dehspande VS, Fleck NA. Isotropic constitutive models for metallic foams. *J Mech Phys Solids* 2000;48(6–7):1253–83.
- [32] Reyes A, Hopperstad OS, Berstad T, Hanssen AG, Langseth M. Constitutive modeling of aluminum foam including fracture and statistical variation of density. *Eur J Mech A – Solids* 2003;22(6):815–35.
- [33] Hanssen AG, Hopperstad OS, Langseth M, Ilstad H. Validation of constitutive models applicable to aluminium foams. *Int J Mech Sci* 2002;44(2):359–406.
- [34] Fang JG, Gao YK, Sun GY, Zhang YT, Li Q. Parametric analysis and multiobjective optimization for functionally graded foam-filled thin-wall tube under lateral impact. *Comput Mater Sci* 2014;90(7):265–75.
- [35] Shan SQ, Wang GG. Metamodeling for high dimensional simulation-based design problems. *J Mech Des* 2010;132(5):051009.
- [36] Song XG, Jung JH, Son HJ, Park JH, Lee KH, Park YC. Metamodel-based optimization of a control arm considering strength and durability performance. *Comput Math Appl* 2010;60(4):976–80.
- [37] Fang JG, Gao YK, Sun GY, Li Q. Multiobjective reliability-based optimization for design of a vehicle door. *Finite Elem Anal Des* 2013;67:13–21.
- [38] Fang H, Rais-Rohani M, Liu Z, Horstemeyer M. A comparative study of metamodeling methods for multiobjective crashworthiness optimization. *Comput Struct* 2005;83(25):2121–36.
- [39] Gao YK, Sun F. Multi-disciplinary optimisation for front auto body based on multiple optimisation methods. *Int J Veh Des* 2011;57(2–3):178–95.
- [40] Sacks J, Welch WJ, Mitchell TJ, Wynn HP. Design and analysis of computer experiments. *Stat Sci* 1989;4(4):409–23.
- [41] Eberhart R, Kennedy J. A new optimizer using particle swarm theory. In: *Proceedings of the sixth international symposium on micro machine and human science*, Nagoya, Japan; 1995.
- [42] Coello CAC, Pulido GT, Lechuga MS. Handling multiple objectives with particle swarm optimization. *IEEE Trans Evol Comput* 2004;8(3):256–79.
- [43] Sun GY, Li GY, Gong ZH, He GQ, Li Q. Radial basis functional model for multi-objective sheet metal forming optimization. *Eng Optim* 2011;43(12):1351–66.